



Enhancing the activity of Pd ensembles on graphene by manipulating coordination environment

Dahong Huang^{a,b,1}, Kali Rigby^{b,1}, Weirui Chen^c, Xuanhao Wu^b, Junfeng Niu^{a,2}, Eli Stavitski^d, and Jae-Hong Kim^{b,2}

Edited by Alexis Bell, University of California, Berkeley, CA; received October 3, 2022; accepted December 28, 2022

Atomic dispersion of metal catalysts on a substrate accounts for the increased atomic efficiency of single-atom catalysts (SACs) in various catalytic schemes compared to the nanoparticle counterparts. However, lacking neighboring metal sites has been shown to deteriorate the catalytic performance of SACs in a few industrially important reactions, such as dehalogenation, CO oxidation, and hydrogenation. Metal ensemble catalysts (M_n), an extended concept to SACs, have emerged as a promising alternative to overcome such limitation. Inspired by the fact that the performance of fully isolated SACs can be enhanced by tailoring their coordination environment (CE), we here evaluate whether the CE of M_n can also be manipulated in order to enhance their catalytic activity. We synthesized a set of Pd ensembles (Pd_n) on doped graphene supports (Pd_n/X-graphene where X = O, S, B, and N). We found that introducing S and N onto oxidized graphene modifies the first shell of Pd_n converting Pd-O to Pd-S and Pd-N, respectively. We further found that the B dopant significantly affected the electronic structure of Pd_n by serving as an electron donor in the second shell. We examined the performance of Pd₀/X-graphene toward selective reductive catalysis, such as bromate reduction, brominated organic hydrogenation, and aqueous-phase CO₂ reduction. We observed that Pd_n/N-graphene exhibited superior performance by lowering the activation energy of the rate-limiting step, i.e., H₂ dissociation into atomic hydrogen. The results collectively suggest controlling the CE of SACs in an ensemble configuration is a viable strategy to optimize and enhance their catalytic performance.

single-atom catalyst | metal ensembles | coordination environment

Single-atom catalysts (SACs), also referred to as atomically dispersed catalysts, have emerged as a promising material design option for various catalytic processes and as an alternative to conventional nanoscale catalysts. They are considered particularly attractive for noble metals since the atomic efficiency can be maximized and the material cost can be significantly reduced (1). SACs are typically strongly bound to a substrate material through interfacial bonds to prevent potential migration on the substrate surface. Otherwise, they tend to aggregate and form nanoparticles due to their high surface free energy (2, 3). Although such atomic dispersion is the core idea of SAC architecture, completely isolating each SAC from other SACs might not be universally desirable. In fact, the distant isolation of SACs to completely eliminate the interaction with other catalytic centers has been reported to have adverse effects on many important catalytic schemes, such as CO oxidation (4, 5), hydrogenation (6, 7), and hydrocarbon oxidation (8, 9). (Fig. 1)

Recent studies present an intriguing strategy to overcome these challenges by placing single-atom catalytic sites close to each other in a small cluster form (8, 10). Such extended single-atom architecture has been referred to as metal ensembles (9), neighboring SACs (11, 12), or fully exposed clusters (13). What distinguishes this structure, called herein as an ensemble with a notation of M_n , from fully isolated SACs (M_1) is the additional bonding/nonbonding interaction between neighboring metal atoms (14, 15). Metals in an ensemble structure otherwise resemble isolated SACs in their coordination environment (CE), i.e., dominant existence of substrate atom bonding to metals (4, 16). In this configuration, neighboring metal atoms provide contiguous positions as active sites, enabling functions that are inefficient with completely isolated SACs (17). For example, simultaneous adsorption of reactants and intermediates on nearby SAC sites (18) can accelerate catalysis without the catalyst poisoning that is prevalent with fully isolated

It is noteworthy that CE can be a deciding factor for the catalytic performance of isolated M₁ sites (20). For example, Cu₁–S₁N₃ exhibits much higher activity toward oxygen reduction than Cu₁-N₄ (21); Fe₁-N₂S₂ is more efficient toward CO₂ reduction than Fe₁-N₂ (22); Fe₁-N₄ exhibits superior activity toward benzene oxidation compared to $Fe_1-N_3C_1$ and $Fe_1-N_2C_2$ (23); and Pt_1-O_4 displays much improved activity over Pt_1-O_6

Significance

Substrate-anchored, single-atom catalysts (SACs) have emerged as a promising alternative to conventional nanocatalysts for various catalytic processes. The catalytic performance of SACs can be controlled by various synthetic strategies, including the manipulation of substrate atoms surrounding metal sites. This study examines whether the coordination environment (CE) of the palladium metal ensemble, a newly identified small-clustered structure with CE resembling that of SAC, can also be tuned by doping nonmetal elements onto the substrate. The results demonstrate that such CE manipulation could decrease the activation energy of the ratelimiting step and achieve efficient H₂ dissociation for several important reductive catalytic schemes, establishing a new strategy to effectively engineer metal ensemble catalysts.

Author contributions: D.H., J.N., and J.-H.K. designed research; D.H. and K.R. performed research; D.H., K.R., W.C., X.W., and E.S. contributed new reagents/analytic tools; D.H., K.R., W.C., X.W., J.N., E.S., and J.-H.K. analyzed data; and D.H., W.C., J.N., E.S., and J.-H.K. wrote the paper.

The authors declare no competing interest.

This article is a PNAS Direct Submission.

Copyright © 2023 the Author(s). Published by PNAS. This article is distributed under Creative Commons Attribution-NonCommercial-NoDerivatives License 4.0 (CC BY-NC-ND).

¹D.H. and K.R. contributed equally to this work.

²To whom correspondence may be addressed. Email: niujf@ncepu.edu.cn or jaehong.kim@yale.edu.

This article contains supporting information online at https://www.pnas.org/lookup/suppl/doi:10.1073/pnas. 2216879120/-/DCSupplemental.

Published February 21, 2023.

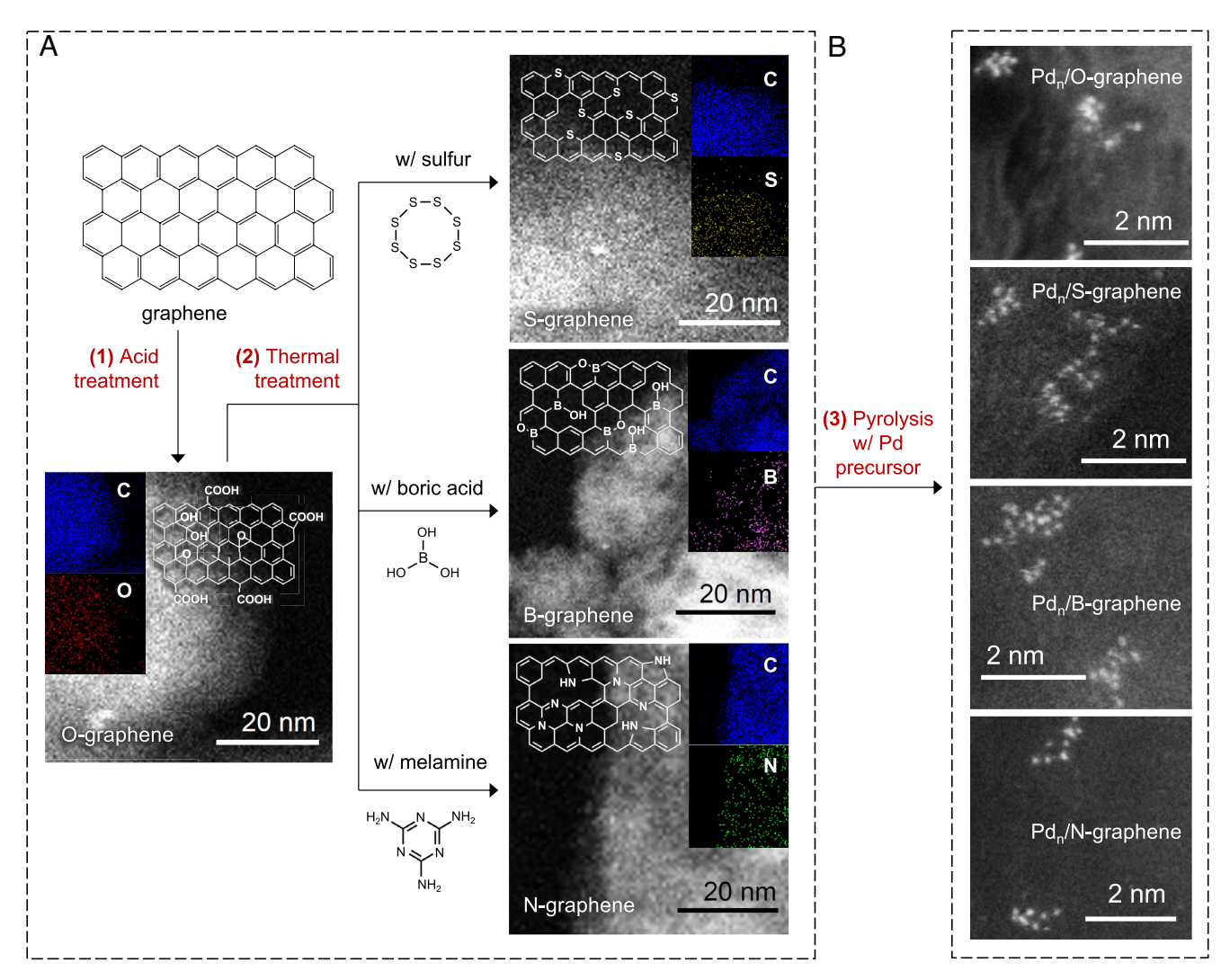


Fig. 1. Schematic illustration of the step-by-step synthesis procedure for Pd_n/X-graphene (X indicates O, S, B, or N): (A) nonmetals doping and EELS mapping of O-graphene, S-graphene, B-graphene, and N-graphene; (B) AC-HAADF-STEM images of Pd_n/O-graphene, Pd_n/S-graphene, Pd_n/B-graphene, and Pd_n/N-graphene.

for CO oxidation (20). These examples of enhancing performances of M_1 by CE manipulation hint that CE of M_n can also be tailored to enhance catalytic performance. However, there is no study yet exploring the CE effect on M_n , likely due to the difficulty of synthesizing M_n with controlled CE (i.e., different substrate atoms binding to M_n). If the atomicity becomes too high, M_n may aggregate into nanoparticles. If the atomicity gets too low, M_n may lose the characteristic interaction between neighboring metal atoms and instead function as M_1 . (Fig. 2)

In this study, we prepared a series of Pd ensemble catalysts (Pd_n) with varying CE by anchoring Pd onto a graphene substrate doped with heteroatoms, such as O, S, B, and N. We selected graphene as the substrate considering a couple of advantageous features: i) high specific surface area (theoretically, 2,600 m² g⁻¹) (24), ensuring uniform distribution of Pd_n and favoring reactant adsorption during catalysis, and ii) facile modification with oxygen-containing groups which can be reductively removed to generate substitutional doping sites (25, 26). We then evaluated the performance of Pd_n for H₂ dissociation into atomic H (H*), a highly active species for many essential reductive reactions, e.g., selective hydrogenation (27, 28), dehalogenation (29), and reduction of CO₂ (30) and NO₃⁻ (31). Our results suggest that these nonmetal dopants can effectively modulate the CE of Pd_n and affect the catalytic performance. We discuss the key role of CE in determining the catalytic performance of Pdn based on detailed X-ray analysis, reaction kinetics evaluation, and density functional theory (DFT) calculations.

Results and Discussion

Synthesis and Structural Characterization of Pd_n/X-Graphene **Catalysts.** We synthesized a set of X-graphene catalysts (X = O, S, S)B, and N) loaded with Pd following a two-step synthesis method. The first step involved substitutional doping of nonmetals onto a graphene substrate. We prepared O-graphene by acid treatment of graphene to introduce oxygen functionalities. X-ray photoelectron spectroscopy (XPS, SI Appendix, Fig. S1) suggests the presence of epoxy and hydroxyl groups on the basal plane and carboxyl and carbonyl groups on the edge of O-graphene (32). We then prepared S-, B-, and N-graphene by thermally treating O-graphene under a reducing atmosphere to remove O-containing groups and substituting S, B, and N using their respective precursors (sulfur, boric acid, and melamine). For S-graphene, we observed only $S 2p_{3/2}/2p_{1/2}$ doublets (164.1/165.3 eV) in the XPS spectrum (SI Appendix, Fig. S2), which can be assigned to C-bound thiophene-like sulfur (C-S-C) (33, 34). The absence of oxidized sulfur species [SO_x, 167.9 eV (33)] confirmed that oxygen was effectively removed from O-graphene. For N-graphene, peaks at 398.3, 399.4, and 401.1 eV in N 1s XPS spectrum (SI Appendix, Fig. S3) can be attributed to pyridinic, pyrrolic, and graphitic N

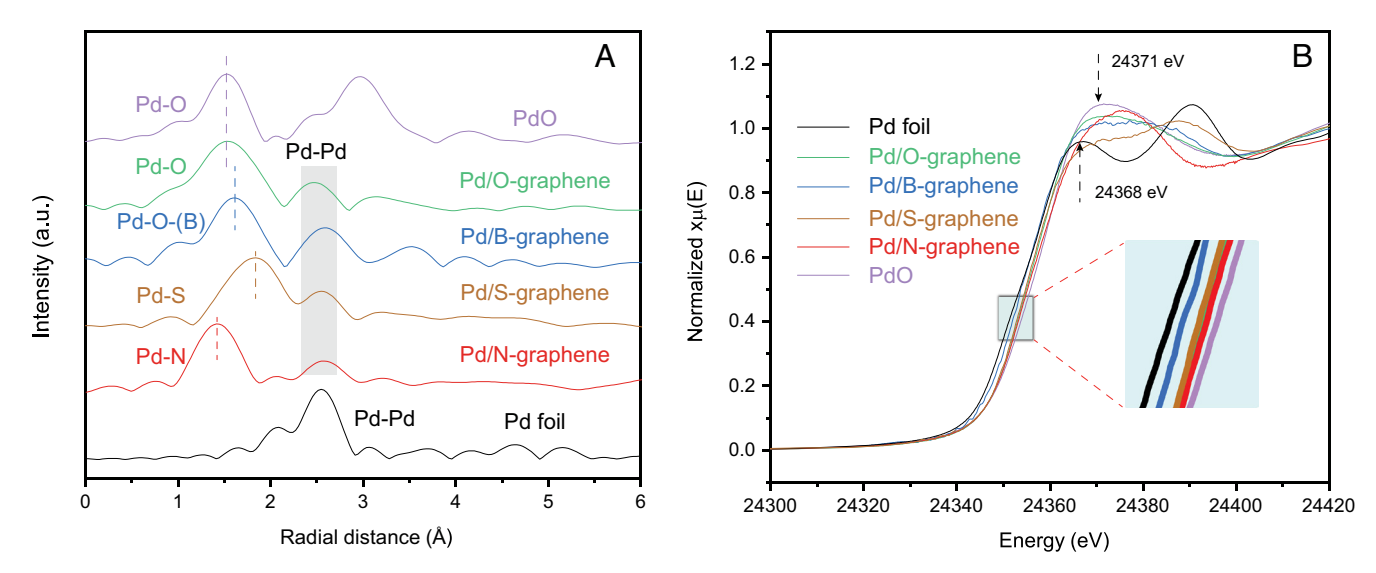


Fig. 2. (*A*) The normalized Pd k^3 -weighted FT-EXAFS of Pd foil, PdO, and Pd_n/X-graphene samples; (*B*) XANES measurements of different Pd_n/X-graphene samples and standards at the Pd K-edge.

species, respectively (35), while an oxidized N peak at 403.3 eV (36) was not observed. In contrast, the B 1s spectrum of B-graphene exhibited a peak at 191.2 eV (*SI Appendix*, Fig. S4) for the O-containing BC₂O structure (25). Considering the absence of oxygen in S- and N-graphenes which underwent the same reductive treatment, O in B-graphene likely originated from the boric acid precursor. Electron energy loss spectroscopy (EELS) mapping (Fig. 1*A*) demonstrates the even distribution of nonmetal dopants on all these graphene substrates. (Fig. 3)

The second step involved $\rm H_2PdCl_4$ precursor physisorption onto these substrates and subsequent pyrolysis under a $\rm N_2$ atmosphere. Raman spectra (*SI Appendix*, Fig. S5) suggest a high concentration of defects on these graphene substrates with the I_D/I_G ratio ranging from 1.09 to 1.11 [I_D represents disordered sp 3 C at ~1,350 cm $^{-1}$; I_G represents lattice sp 2 C at ~1,580 cm $^{-1}$ (37,38)] which serve as trapping sites to stabilize Pd. Pyrolysis conditions were optimized to obtain Pd $_n$ morphology since too low of a temperature can lead to residual Cl (*SI Appendix*, Fig. S6) and

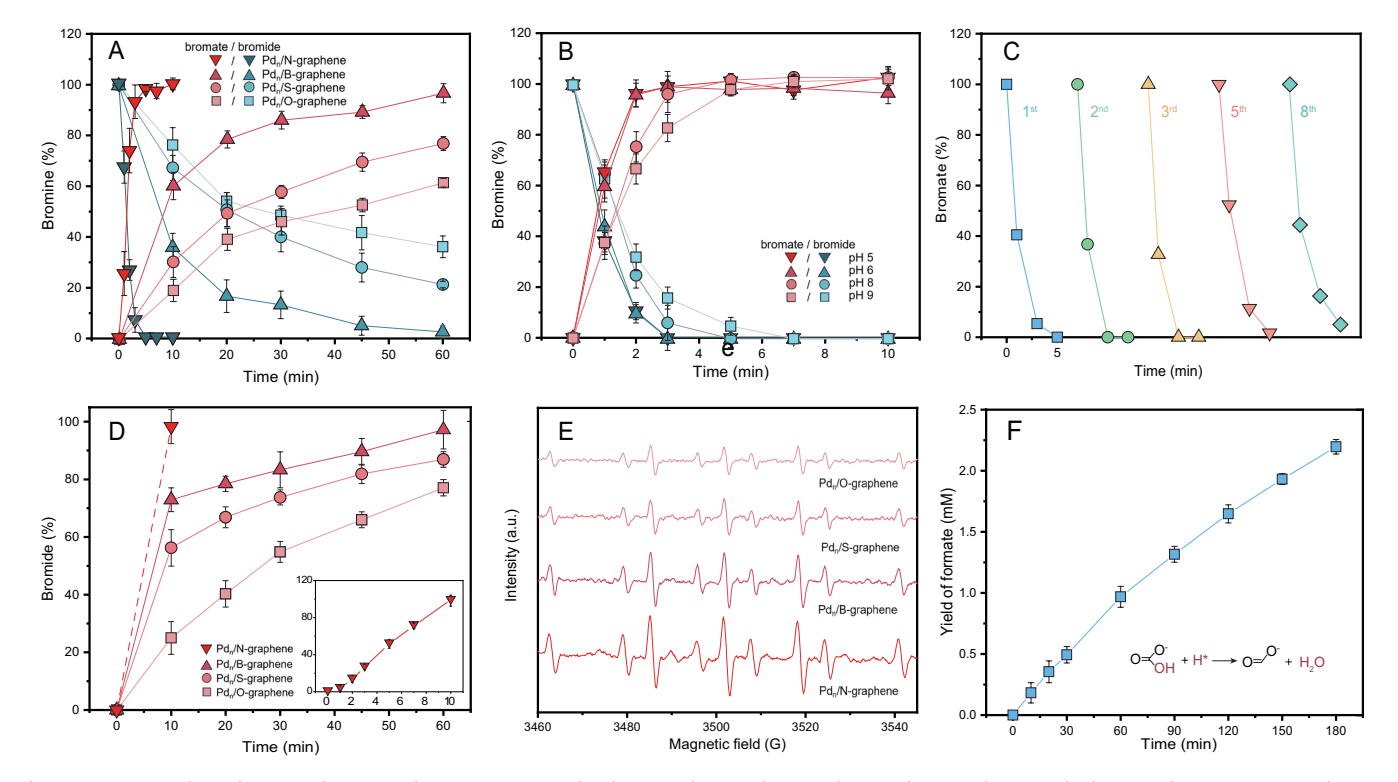


Fig. 3. (*A*) Kinetic plots of BrO_3^- reduction and Br^- generation with Pd_n/O -graphene, Pd_n/S -graphene, Pd_n/B -graphene, and Pd_n/N -graphene. (*B*) BrO_3^- reduction with Pd_n/N -graphene catalyst under various pH conditions. (*C*) BrO_3^- reduction with Pd_n/N -graphene catalyst after repetitive cycling. (*D*) Debromination of TBBPA with Pd_n/O -graphene, Pd_n/S -graphene, Pd_n/S -graphene, and Pd_n/N -graphene catalysts; the *Inset* is a kinetic plot using Pd_n/N -graphene within 10 min. (*E*) EPR spectra with Pd_n/O -graphene, Pd_n/S -graphene, and Pd_n/N -graphene, using DMPO as the probe to identify the existence of Pd_n/S -graphene, and Pd_n/S -graphene, and Pd_n/S -graphene, using DMPO as the probe to identify the existence of Pd_n/S -graphene. Experimental conditions: catalysts (0.5 g Pd_n/S -graphene) or Pd_n/S -graphene. Experimental conditions: catalysts (0.5 g Pd_n/S -graphene) or Pd_n/S -graphene. Experimental conditions: catalysts (0.5 g Pd_n/S -graphene) or Pd_n/S -graphene.

insufficient reduction of Pd precursor (39), while too high of a temperature can lead to the redistribution into Pd₁ (40). In addition, a gentle heating rate (2 °C/min) was applied to avoid too rapid precursor reduction and consequential Pd nanoparticle growth (41).

Aberration-corrected high-angle annular dark-field scanning transmission electron microscopy (AC-HAADF-STEM) images (Fig. 1 B and SI Appendix, Fig. S7) provided visual confirmation of the ensemble configuration of Pd at atomic scale (referred to as Pd_n/X-graphene hereafter) and the absence of Pd nanoparticles. Fourier-transformed extended X-ray absorption fine structure spectroscopy (FT-EXAFS) analysis further confirmed that Pd_n/X-graphene appeared drastically different compared to metallic Pd (Pd foil), which showed only one dominant Pd–Pd peak at 2.61 Å (Fig. 2A). The FT-EXAFS spectra of Pd_n/O-graphene featured one distinct peak at 1.52 Å in the first shell, which matched well with Pd-O peak in the PdO reference. The slight peak shift of Pd-O to 1.59 Å in Pd_n/B-graphene likely resulted from the influence of B, which causes an asymmetrical expansion of the first shell (42). In the Pd_n/S-graphene catalyst, the main peak at a much higher radial distance (1.82 Å) was attributed to the Pd-S shell (43). Finally, the peak at 1.45 Å in Pd_n/N-graphene was assigned to the Pd-N coordination (44). Pd-Pd peaks shifted slightly among different Pd_n/X-graphene samples (gray box in Fig. 2A), which is likely associated with the specific CE offered by different nonmetal dopants (Fig. 4).

We observed that the Pd K-edge absorption energy in the X-ray absorption near-edge spectroscopy (XANES) spectra (Fig. 2B) was in the order: metallic Pd < Pd_n/B-graphene < Pd_n/O-graphene \approx Pd_n/S-graphene \approx Pd_n/N-graphene < PdO. This correlates with the oxidation state of the metal (45), where Pd in Pd_n/B-graphene would be in a more reduced state compared to Pd in other Pd_n/X-graphenes. Consistently, we observed that the first peak of the XANES derivative was positioned at 24,351 eV for Pd_n/B-graphene, which is at lower energy than 24,352 eV for Pd_n/O-, Pd_n/S-, and Pd_n/N-graphenes (*SI Appendix*, Fig. S8). This result

corroborates a recent work that reported the increased oxidation state of metal centers induced by electron-withdrawing F doping on Pd-hosting substrate, even when F does not directly bind to Pd (46). The results so far collectively suggest that i) doping S or N replaces Pd–O coordination in the first shell of Pd_n by Pd–S or Pd–N coordination and ii) doping B into graphene retains Pd–O coordination in the Pd_n but with lower Pd oxidation state.

We postulate that Pd ensembles exist in more than one configuration and have a distribution of atomicity (e.g., few to several single-atom Pd centers). We therefore evaluated the average CE of Pd in ensembles based on structural parameters obtained from fitting EXAFS and XPS results (SI Appendix, Figs. S9 and S10) (47). For example, the average CN of Pd-Pd shell in all Pd_p/Xgraphenes is ~3 (SI Appendix, Table S1), indicating that each Pd atom binds, on average, to 3 other Pd atoms within each Pd_n. We therefore propose tetrahedron-structured Pd₄ as a dominant Pd_n form (48) among other possible structures (e.g., inverted tetrahedron or tetrahedron aligned to X-graphene layer along the edge/ facet) based on best fitting of EXAFS data. Although different dopants would affect the metal-support interaction, (49, 50), we found that the surface energy of the Pd atom and the resultant thermodynamic driving force to aggregate were not significantly influenced, as evidenced by the average nuclearity of Pd4 in all Pd_n/X-graphenes. We then employed DFT calculations to estimate the Gibbs energy of formation among all possible structures to construct the most probable structure for each Pd_n/X-graphene as shown in *SI Appendix*, Table S2. For Pd_n/O-graphene, Pd would be anchored via C-O-Pd (51). For Pd_n/B-graphene, we predict that Pd also binds with O (C2-B-O-Pd) covalently. This covalent bond will likely have a partial ionic bond character due to the much higher electronegativity of O (3.44) than B (2.04) and C (2.55) in BC₂O moiety. For Pd_n/S-graphene, we propose C₂–S–Pd structure, since S atom in C₂-S has been demonstrated to be able to form an additional bond with a metal atom (52). For Pd_n/N-graphene, we propose Pd coordinates with pyrrolic N (i.e., C₂-N-Pd), not graphitic nor pyridinic N. We considered that

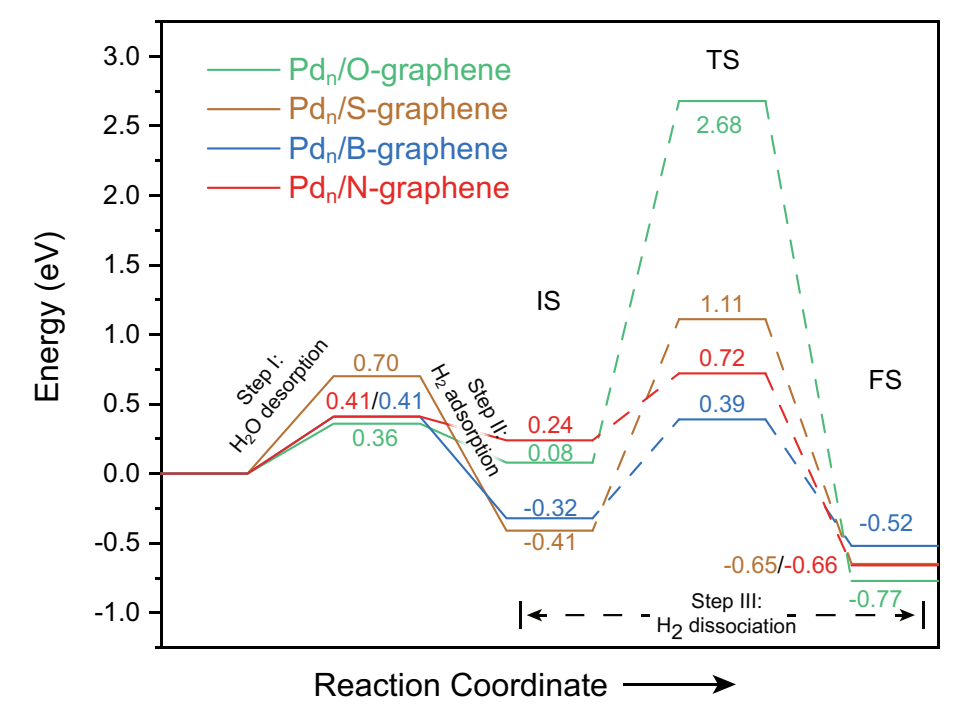


Fig. 4. DFT calculated minimum energy paths for H* formation on various Pd_n moieties with the engineered CE. IS stands for initial state, TS for transition state, and FS for final state. All theoretical models involved in the reaction process are presented in *SI Appendix*, Figs. S21–S24.

i) graphitic N in coordinative saturation has been experimentally and theoretically demonstrated to be unable to bind with Pd (53), and ii) pyridinic N is in a much lower concentration than pyrrolic N (SI Appendix, Fig. S3) and has been demonstrated to be less favorable as N coordination species (54).

Relationship between CE and Catalytic Performance. We investigated the performance of Pd_n/X-graphenes for catalytic reduction involving H₂ dissociation and H* generation. We selected bromate (BrO₃⁻) as a representative target for reductive decontamination, considering its prevalent occurrence as a disinfection byproduct and serious public health threat as a Group 2B carcinogen (55, 56). We observed a near-complete bromine mass balance throughout the reaction (stoichiometric generation of Br from the destruction of BrO₃) (SI Appendix, Figs. S11 and S12). This indicates that all BrO₃ was selectively reduced to Br by Pd_n/X-graphene catalysts, without the accumulation of intermediates such as BrO₂ and BrO which could form depending on the reduction pathways (57).

However, the kinetics of BrO₃ depended on the type of heteroatoms that affect CE of Pd in Pdn; the kinetics were in the order of Pd_n/O-graphene < Pd_n/S-graphene < Pd_n/N-graphene < Pd_n/Ngraphene (Fig. 3A). The Pd_n/N-graphene exhibited the fastest kinetics, with over 95% BrO₃ reduction within 3 min (SI Appendix, Fig. S13). We additionally compared the turnover frequency (TOF, per Pd atom basis) to those of other reported catalysts (summarized in SI Appendix, Tables S3 and S4 and Figs. S14 and S15) and found that Pd_n/N-graphene exhibited the highest TOF (up to 11.2 min⁻¹) under neutral pH condition. Due to the low activity of conventional Pd-based catalysts toward H* generation, acidic conditions are typically required to enhance BrO₃ adsorption onto the positively charged surface and thereby improve the H* utilization efficiency (58, 59). The superior activity of Pd_n/N-graphene rendered a broad pH-adaptability (Fig. 3B), wherein the electrostatic adsorption between BrO₃ and catalyst was no longer necessary. EXAFS results demonstrate that all Pd_n/ X-graphene catalysts retained their original property even after being stored in H2-saturated solution for 1 wk (SI Appendix, Fig. S16). We filtered the suspension after the storage and confirmed no Pd leaching [i.e., Pd in the permeate was below the detection limit of inductively coupled plasma mass spectrometry (ICP-MS) analysis]. The catalysts recovered by the filter maintained the original bromate reduction capability, confirming the dominant role of heterogeneous catalysis without the involvement of dissolved Pd species (SI Appendix, Fig. S17). Finally, the activity of Pd_n/N-graphene was maintained over eight cycles of repetitive use (Fig. 3*C*).

Electron paramagnetic resonance (EPR) spectra obtained using 5,5-dimethyl-1-pyrroline N-oxide (DMPO) as the probe (Fig. 3D) showed a series of nine characteristic peaks for all Pd_n/ X-graphene samples, which indicate the occurrence of H* (60). Although the relative intensities of the DMPO/H* adducts cannot provide a quantitative correlation, a stronger intensity can generally be interpreted as a higher concentration of H*. Relative intensities of the H* signal are in the order of Pd_n/O-graphene < Pd_n/S-graphene < Pd_n/B-graphene < Pd_n/N-graphene, which matches well with the increasing reaction kinetics. We consequently infer that the highest activity of Pd_n/N-graphene results from the most efficient H* generation. Considering that Pd atoms in Pd_n/O-graphene, Pd_n/S-graphene, and Pd_n/N-graphene are all similar in oxidation state (Fig. 2B), size (with an atomicity of ~4), and structure (SI Appendix, Tables S1 and S2), we postulate that the difference in H₂ dissociation activity is mostly influenced by the Pd-X coordination environment. Such influence of support

on the catalytic activity of metal sites has also been observed when Ir clusters were loaded on different substrates such as MgO and γ -Al₂O₃ (61).

To expand the potential applications to other environmentally relevant catalytic schemes, we additionally examined the reductive debromination of tetrabromobisphenol A (TBBPA), one of the most widely used brominated flame retardants. TBBPA is a potent endocrine disrupter and a widespread water pollutant (62, 63). The optimized Pd_p/N-graphene also exhibited fast kinetics, achieving around 100% TBBPA debromination within 10 min of catalysis (Fig. 3E and SI Appendix, Figs. S18). As another example, we evaluated the reduction of bicarbonate (HCO₃⁻) (Fig. 3F) (64), where H* has been identified as the main reductant (65). Pd_n/Ngraphene efficiently converted HCO_3^- into value-added formate (HCO_2^-) with a TOF of 45 h⁻¹ (*SI Appendix*, Fig. S19), which is much higher than TOFs by previously reported catalysts (SI Appendix, Table S5 and Fig. S20). Such Pd-catalyzed HCO₃ reduction has demonstrated 100% selectivity without the generation of any other products (e.g., CH₄, CO, methanol, or acetate) (66, 67), avoiding a downstream process for product separation.

Reaction Mechanisms. We performed DFT calculations to examine how Pdn with different CEs differently interact with H₂ and form H*. The lowest-energy pathways for the overall H* generation process for different Pdn/X-graphenes are shown in (Fig. 4). After the endothermic H₂O desorption from Pd atom in Pd_n, H₂ adsorbs onto this Pd site. The H–H bond of adsorbed H₂ (initial state, IS) is stretched from 0.74 Å of the H₂ molecule due to its σ-bonding to 4d orbitals of Pd atoms (48). The DFT results (SI Appendix, Figs. S21 to S24 and Table S6) suggest that the length of H-H bonds in the IS varies from 0.82 to 0.90 Å depending on X in Pd_n/X-graphene. In addition, the distance between Pd (from 1.68 to 1.86 Å) and H as well as the orientation of H₂ on Pd_n are also different.

The final state (FS), defined as two fully-separated H* atoms adsorbed onto Pd_n, also depends on the identity of X in Pd_n/Xgraphene (SI Appendix, Figs. S21 to S24). A Bader analysis (SI Appendix, Table S7) demonstrates that both H* atoms in FS states are negatively charged, resulting from homolytic H2 dissociation (68). In Pd_n/O-graphene, one H* diffuses to the center of the triangle facet by binding to three Pd atoms, and the other H* diffuses to the middle of the Pd-Pd edge by binding to two Pd atoms. In Pd_n/B-graphene, two H* atoms bind to the same Pd atom. Though two separated H* atoms diffuse to two Pd-Pd edges in both Pd_n/S-graphene and Pd_n/N-graphene, the location of the Pd-Pd edge is different due to the specific Pd_n configuration affected by the dopant species. The activation energy from IS to transition state (TS), as estimated by simulating and scanning possible states, varies significantly depending on the catalysts: Pd_n/Ngraphene (0.48 eV) < Pd_n/B-graphene (0.71 eV) < Pd_n/S-graphene $(1.52 \text{ eV}) < \text{Pd}_n/\text{O-graphene}$ (2.60 eV). The sequence of activation energy offers a rational interpretation for the experimentally observed variations in reaction kinetics (i.e., Pd_n/N-graphene > Pd_n/B-graphene > Pd_n/S-graphene > Pd_n/O-graphene). In order to experimentally confirm H₂ dissociation as the rate-limiting step, we evaluated the kinetic isotope effect (KIE) using D₂ as an alternative hydrogen source. As shown in SI Appendix, Fig. S25, D2 substitution led to a primary KIE (k_H/k_D) of 1.74, since the lower zero-point energy of D2 resulted in a higher activation energy of D₂ dissociation.

We would like to note that the above activation energies can only be used to qualitatively compare the activities of Pd_n/X-graphenes. It is difficult to build a quantitative relationship between calculated energy barriers and observed kinetics (69) since representative DFT models cannot fully capture the inherent complexity of real metal ensembles (47, 70). We propose that further research should focus on improving synthetic strategies, for example, by optimizing nonmetal dopants or using organic ligands, in order to synthesize $M_{\rm n}$ with uniform atomicity and thereby alleviate the gap between theoretical predictions and experimental observations.

Conclusions

This study presents the precise control of the CE of Pd ensembles and the resulting enhancement of catalytic performance by O, S, B, and N doping of a graphene substrate. We observed that reconstructing the Pd-O coordination in the first shell of Pd_n into Pd-S/N through S/N doping significantly affects the catalytic performance. Even when Pd-O in the first shell remains unchanged after B doping, B substantially tunes the electronic structure of Pd_n centers as an electron donor in the second shell, leading to a much higher activity. Computational results reveal that the activation energy of H2 dissociation as the rate-limiting step highly depends on the CE of Pd_n and that the highest catalytic activity of Pd_n/N-graphene results from enhanced H₂ dissociation. Our findings highlight the importance of CE manipulation for Pd_n, similar to isolated Pd₁, since the identity of substrate atom that binds to the metal affects the geometric/electronic structure of metal centers and thus determines the overall reaction kinetics. Our study calls for future efforts to establish a fundamental understanding of the CE effect on a wider range of M_n catalysts beyond Pd_n and additional strategies to tailor CE with the goal of fully exploiting the catalytic capability of SAC materials.

Materials and Methods

Materials. All chemicals used in the experiments were of reagent grade or higher and were used as received without further purification. Tetrabromobisphenol A ($C_{15}H_{12}Br_4O_2$, TBBPA) and Bisphenol A ($C_{15}H_{16}O_2$, BPA) were obtained from J&K Scientific. Sodium bromate (NaBrO₃), boric acid (H_3BO_3), sulfur (S), melamine ($C_3H_6N_6$), sodium bicarbonate (NaHCO₃), sodium formate (NaCOOH), sulfate acid (H_2SO_4), and nitric acid (HNO_3) are purchased from Sigma-Aldrich. Graphene nanoplatelet was obtained from Strem Chemicals. All aqueous solutions were prepared with ultrapure/deionized water obtained from a Milli-Q system.

Catalyst Synthesis.O-graphene preparation. First, 0.5 g graphene nanoplatelets was dispersed in 100 mL mixed acid solution (HNO $_3$:H $_2$ SO $_4$ = 70:30) in a round-bottom flask. This flask was subsequently connected to a reflux system under stirring and heated in an oil bath at 90 °C for 6 h. After cooling down to the room temperature, O-graphene was separated by centrifugation, washed with deionized water (until neutral pH), and dried in an oven at 80 °C.

B-graphene, S-graphene, and N-graphene syntheses. O-graphene was well-ground together with boric acid (sulfur or melamine, ten times the weight of O-graphene) and then heated at $800 \,^{\circ}$ C for $2 \, h$ (4 h for boron) with a heating rate of $2 \,^{\circ}$ C/min in a tube furnace under a H_2/Ar (5:95) atmosphere.

Syntheses of Pdn with various CE. First, 80 mg O-graphene (B-graphene, S-graphene, or N-graphene) was dispersed into 40 mL deionized water under probe sonication for 0.5 h, followed by the addition of $375 \mu L H_2 PdCl_4$ (10 mM). The mixture was shaken at 300 rpm for 24 h and then dried at 80 °C in the oven.

- H. Xu et al., Entropy-stabilized single-atom Pd catalysts via high-entropy fluorite oxide supports. Nat. Commun. 11, 1–9 (2020).
- K. Liu et al., Strong metal-support interaction promoted scalable production of thermally stable single-atom catalysts. Nat. Commun. 11, 1-9 (2020).
- D. Huang et al., Conflicting roles of coordination number on catalytic performance of single-atom Pt catalysts. ACS Catal. 11, 5586–5592 (2021).
- H. Wang et al., Surpassing the single-atom catalytic activity limit through paired Pt-O-Pt ensemble built from isolated Pt₁ atoms. Nat. Commun. 10, 1–12 (2019).
- H. Gu et al., Adjacent single-atom irons boosting molecular oxygen activation on MnO₂. Nat. Commun. 12, 1–9 (2021).

The obtained powder was then well-ground and moved to a crucible, heated at 800 °C for 2 h with a heating rate of 2 °C/min in a tube furnace under a $\rm N_2$ atmosphere. The Pd loading amount was determined by ICP-MS: 0.45 wt%, 0.43 wt%, 0.47 wt%, 0.46 wt% for Pd_n/O-graphene, Pd_n/S-graphene, Pd_n/B-graphene, and Pd_n/N-graphene, respectively.

Catalyst Characterization. HAADF-STEM images were taken on a Titan Themis Z STEM (ThermoFisher Scientific) operated at 200 kV, coupled with a probe aberration-corrector to improve imaging spatial resolution to less than 1 Å. The X-ray absorption spectroscopy spectra at Pd K-edge were measured at Inner Shell Spectroscopy beamline of the National Synchrotron Light Source II at Brookhaven National Laboratory (60), using a Si (111) double-crystal monochromator and a passivated implanted planar silicon (PIPS) fluorescence detector at room temperature, with energy calibrated using Pd foil. The catalyst samples were pressed into pellets and sealed in Kapton films for XAFS measurements. XAFS data were analyzed using Athena and Artemis software for conversion of raw data to $\mu(E)$ spectra, background subtraction and normalization, Fourier transformation and plotting, and fitting in k-space and R-space.

Evaluation of Catalytic Performance. BrO $_3^-$ reduction, TBBPA debromination, and HCO $_3^-$ reduction tests were conducted in a serum glass bottle sealed with rubber septa at room temperature (25 °C). The suspension containing 0.5 g/L catalyst and 50 ppm TBBPA (50 ppm BrO $_3^-$ or 0.5 M HCO $_3^-$) was sonicated or 15 min to ensure the dynamic adsorption/desorption equilibrium (*SI Appendix*, Figs. S26 and S27). Hydrogen gas was continuously sparged into the bottle at 5 mL/min throughout the whole reaction. Aliquots (250 μ L) were taken at defined time points from the sample solutions by a syringe and immediately filtered by a polyethersulfone filter. To evaluate the catalyst stability, catalysts were collected and washed with ethanol and water after each cycle and redispersed in 50 ppm BrO $_3^-$ solution for recycling tests. All experiments were conducted in triplicates and the error bars in figures represent the SD from the mean value.

Quantification of Reactants and Final Products. Aliquots were filtered, and 200 µL solution was diluted to 5 mL deionized water for ion chromatography (IC, Dionex LC20) tests, equipped with Dionex IonPac[™] AG14A column. NaBrO₃, NaBr, NaHCO₃, and NaCOOH standard solutions were used to calibrate the peak area in relation to concentration.

Data, Materials, and Software Availability. Supporting figures and tables described within the manuscript are provided. All study data are included in the article and/or *SI Appendix*.

ACKNOWLEDGMENTS. We thank the National Natural Science Foundation for Youth from China (No. 52100172). This study was partly supported the NSF Nanosystems Engineering Research Center for Nanotechnology-Enabled Water Treatment (EEC-1449500) and NSF Division of Chemical, Bioengineering, Environmental, and Transport Systems (CBET) Grant #1955793. This research used beamline 8-ID (Inner Shell Spectroscopy, ISS) of the National Synchrotron Light Source II, a U.S. Department of Energy (DOE) Office of Science User Facility operated for the DOE Office of Science by Brookhaven National Laboratory under Contract No. DE-SC0012704. We are grateful to J. Karosas and T. Hedtke (Yale) for help with IC and ICP-MS.

Author affiliations: ^aCollege of Environmental Science and Engineering, North China Electric Power University, Beijing 102206, China; ^bDepartment of Chemical and Environmental Engineering, Yale University, New Haven, CT 06520; ^cSchool of Environmental Science and Engineering, Guangdong University of Technology, Guangzhou 510006, China; and ^dNational Synchrotron Light Source-II, Brookhaven National Laboratory, Upton, NY 11973

- M. D. Rossell et al., Magnetite-supported palladium single-atoms do not catalyse the hydrogenation of alkenes but small clusters do. Catal. Sci. Technol. 6, 4081–4085 (2016).
- L. Liu et al., Determination of the evolution of heterogeneous single metal atoms and nanoclusters under reaction conditions: Which are the working catalytic sites? ACS Catal. 9, 10626–10639 (2019).
- H. Jeong et al., Fully dispersed Rh ensemble catalyst to enhance low-temperature activity. J. Am. Chem. Soc. 140, 9558-9565 (2018).
- H. Jeong et al., Highly durable metal ensemble catalysts with full dispersion for automotive applications beyond single-atom catalysts. Nat. Catal. 3, 368–375 (2020).
- Z. Liu et al., Tuning the selectivity of catalytic nitriles hydrogenation by structure regulation in atomically dispersed Pd catalysts. Nat. Commun. 12, 1–8 (2021).

- 11. H. Li et al., Synergetic interaction between neighbouring platinum monomers in CO₂ hydrogenation. Nat. Nanotechnol. 13, 411-417 (2018).
- C. Chu et al., Neighboring Pd single atoms surpass isolated single atoms for selective hydrodehalogenation catalysis. Nat. Commun. 12, 1-7 (2021).
- C. Dong et al., Fully exposed palladium cluster catalysts enable hydrogen production from nitrogen heterocycles. Nat. Catal. 5, 485-493 (2022).
- L Jiao et al., Non-bonding interaction of neighboring Fe and Ni single-atom pairs on MOF-derived N-doped carbon for enhanced CO₂ electroreduction. J. Am. Chem. Soc. **143**, 19417–19424 (2021).
- X. Zhang et al., A stable low-temperature H₂-production catalyst by crowding Pt on α-MoC. Nature **589**. 396-401 (2021).
- S. Ji $\it{et\,al.}$, Confined pyrolysis within metal-organic frameworks to form uniform \it{Ru}_3 clusters for efficient oxidation of alcohols. J. Am. Chem. Soc. 139, 9795–9798 (2017).
- J. Resasco et al., Relationship between atomic scale structure and reactivity of Pt catalysts: Hydrodeoxygenation of m-cresol over isolated Pt cations and clusters. ACS Catal. 10, 595-603
- 18. H. Jeong, S. Shin, H. Lee, Heterogeneous atomic catalysts overcoming the limitations of single-atom catalysts. ACS Nano 14, 14355-14374 (2020).
- K. Ding et al., Identification of active sites in CO oxidation and water-gas shift over supported Pt catalysts. Science 350, 189-192 (2015).
- L. DeRita et al., Structural evolution of atomically dispersed Pt catalysts dictates reactivity. Nat. Mater.
- H. Shang et al., Engineering unsymmetrically coordinated Cu-S₁N₃ single atom sites with enhanced oxygen reduction activity. Nat. Commun. 11, 1-11 (2020).
- S. Cao et al., Can N, S cocoordination promote single atom catalyst performance in CO₂RR? Fe-N₂S₂
- porphyrin versus Fe- N_4 Porphyrin. *Small* **17**, 2100949 (2021). Y. Pan *et al.*, Regulating the coordination structure of single-atom Fe- N_x C_y catalytic sites for benzene oxidation. Nat. Commun. 10, 1-11 (2019).
- S. Stankovich et al., Graphene-based composite materials. Nature 442, 282-286 (2006)
- X. Yu et al., Boron-doped graphene for electrocatalytic N₂ reduction. Joule 2, 1610-1622 (2018). 25
- R. Kumar et al., Heteroatom doped graphene engineering for energy storage and conversion. Mater. 26 Today 39, 47-65 (2020).
- G. Zhao, T. Liu, B. Wu, B. Chen, C. Chu, Constructing the support as a microreactor and regenerator for highly active and in situ regenerative hydrogenation catalyst. Adv. Funct. Mater. 31, 2100971
- Y. Ren et al., Unraveling the coordination structure-performance relationship in Pt₁/Fe₂O₃ singleatom catalyst. Nat. Commun. 10, 1-9 (2019).
- D. Huang et al., Elucidating the role of single-atom Pd for electrocatalytic hydrodechlorination. Environ. Sci. Technol. 55, 13306-13316 (2021).
- W. Lin, K. M. Stocker, G. C. Schatz, Mechanisms of hydrogen-assisted CO₂ reduction on nickel. *J. Am.* Chem. Soc. 139, 4663-4666 (2017).
- S. Guo et al., Insights into nitrate reduction over indium-decorated palladium nanoparticle catalysts. ACS Catal. 8, 503-515 (2018).
- $\hbox{T. F. Yeh, C. Y. Teng, S. J. Chen, H. Teng, Nitrogen-doped graphene oxide quantum dots as}\\$ photocatalysts for overall water-splitting under visible light Illumination. Adv. Mater. 26, 3297-3303 (2014).
- Q. Pang et al., A nitrogen and sulfur dual-doped carbon derived from polyrhodanine@cellulose for advanced lithium-sulfur batteries. Adv. Mater. 27, 6021-6028 (2015).
- J. Liang, Y. Jiao, M. Jaroniec, S. Z. Qiao, Sulfur and nitrogen dual-doped mesoporous graphene electrocatalyst for oxygen reduction with synergistically enhanced performance. Angew. Chem. Int. Ed. 51, 11496-11500 (2012).
- J. Zou et al., Facile steam-etching approach to increase the active site density of an ordered porous Fe-N-C catalyst to boost oxygen reduction reaction. ACS Catal. 12, 4517-4525 (2022).
- S. Zhou et al., Pd single-atom catalysts on nitrogen-doped graphene for the highly selective photothermal hydrogenation of acetylene to ethylene. Adv. Mater. 31, 1900509 (2019).
- L. Bao et al., Spatially resolved bottom-side fluorination of graphene by two-dimensional substrate patterning. Angew. Chem. Int. Ed. 59, 6700-6705 (2020).
- J. M. Englert et al., Scanning-Raman-microscopy for the statistical analysis of covalently functionalized graphene. ACS Nano 7, 5472–5482 (2013).
- X. P. Yin et al., Engineering the coordination environment of single-atom platinum anchored on graphdiyne for optimizing electrocatalytic hydrogen evolution. Angew. Chem. Int. Ed. 57, 9382-9386 (2018).
- S. Wei et al., Direct observation of noble metal nanoparticles transforming to thermally stable single atoms. Nat. Nanotechnol. 13, 856-861 (2018).
- S. Gao et al., Synthesis of high-entropy alloy nanoparticles on supports by the fast moving bed pyrolysis. Nat. Commun. 11, 1-11 (2020).

- 42. J. Qin et al., Altering ligand fields in single-atom sites through second-shell anion modulation boosts the oxygen reduction reaction. J. Am. Chem. Soc. 144, 2197-2207 (2022).
- T. Matsui, M. Harada, K. K. Bando, M. Toba, Y. Yoshimura, EXAFS study on the sulfidation behavior of Pd, Pt and Pd-Pt catalysts supported on amorphous silica and high-silica USY zeolite. Appl. Catal. A Gen. 290, 73-80 (2005).
- 44. L. Han et al., Modulating single-atom palladium sites with copper for enhanced ambient ammonia electrosynthesis. Angew. Chem. Int. Ed. 133, 349-354 (2021).
- Y. Han et al., Hollow N-doped carbon spheres with isolated cobalt single atomic sites: Superior electrocatalysts for oxygen reduction. J. Am. Chem. Soc. 139, 17269–17272 (2017).
- J. Chang et al., Improving Pd-N-C fuel cell electrocatalysts through fluorination-driven rearrangements of local coordination environment. *Nat. Energy* **6**, 1144–1153 (2021).
- X. Chen et al., Regulating coordination number in atomically dispersed Pt species on defect-rich graphene for n-butane dehydrogenation reaction. Nat. Commun. 12, 1-9 (2021).
- Ĭ. Cabria, M. López, S. Fraile, J. Alonso, Adsorption and dissociation of molecular hydrogen on palladium clusters supported on graphene. J. Phys. Chem. C 116, 21179–21189 (2012).
- C. T. Campbell, S. C. Parker, D. E. Starr, The effect of size-dependent nanoparticle energetics on catalyst sintering. Science 298, 811-814 (2002).
- C.T. Campbell, The energetics of supported metal nanoparticles: Relationships to sintering rates and catalytic activity. Acc. Chem. Res. 46, 1712-1719 (2013).
- H. Yan et al., Single-atom Pd₁/graphene catalyst achieved by atomic layer deposition: Remarkable performance in selective hydrogenation of 1, 3-butadiene. J. Am. Chem. Soc. 137, 10484-10487
- D. Chen et al., A tandem strategy for enhancing electrochemical CO₂ reduction activity of single-atom Cu-S₁N₃ catalysts via integration with Cu nanoclusters. Angew. Chem. Int. Ed. 60, 24022-24027 (2021).
- R. Arrigo et al., Nature of the N-Pd interaction in nitrogen-doped carbon nanotube catalysts. ACS Catal. 5, 2740-2753 (2015).
- Y. Xiong et al., Single-atom Fe catalysts for Fenton-like reactions: Roles of different N species. Adv. Mater. 34, 2110653 (2022).
- L. Xie, C. Shang, Role of humic acid and quinone model compounds in bromate reduction by zerovalent iron. Environ. Sci. Technol. 39, 1092-1100 (2005).
- J. Qiao, L. Feng, H. Dong, Z. Zhao, X. Guan, Overlooked role of sulfur-centered radicals during bromate reduction by sulfite. Environ. Sci. Technol. 53, 10320-10328 (2019).
- Q. Xiao et al., An overview of advanced reduction processes for bromate removal from drinking water: Reducing agents, activation methods, applications and mechanisms. J. Hazard. Mater. 324,
- J. Zhou, X. Zhou, L. Li, Q. Chen, Enhanced liquid phase catalytic hydrogenation reduction of bromate over Pd-on-Au bimetallic catalysts. *Appl. Catal. A Gen.* 562, 142–149 (2018).
 H. Chen *et al.*, Aqueous bromate reduction by catalytic hydrogenation over Pd/Al₂O₃ catalysts. *Appl.*
- Catal. B Environ. 96, 307-313 (2010).
- R. Mao et al., Dechlorination of trichloroacetic acid using a noble metal-free graphene-Cu foam electrode via direct cathodic reduction and atomic H. Environ. Sci. Technol. 50, 3829-3837 (2016).
- 61. A. Argo, J. Odzak, F. Lai, B. Gates, Observation of ligand effects during alkene hydrogenation catalysed by supported metal clusters. Nature 415, 623-626 (2002).
- Y. Ding, L. Zhu, N. Wang, H. Tang, Sulfate radicals induced degradation of tetrabromobisphenol A with nanoscaled magnetic CuFe₂O₄ as a heterogeneous catalyst of peroxymonosulfate. *Appl. Catal.* B Environ. 129, 153-162 (2013).
- C. Gu et al., Biogenic Fenton-like reaction involvement in cometabolic degradation of tetrabromobisphenol A by Pseudomonas sp. fz. Environ. Sci. Technol. 50, 9981-9989 (2016).
- D. He et al., Hydrothermal synthesis of long-chain hydrocarbons up to C₂₄ with NaHCO₃ assisted stabilizing cobalt. Proc. Natl. Acad. Sci. U.S.A. 118, e2115059118 (2021).
- X. Wang, H. Shi, J. H. Kwak, J. Szanyi, Mechanism of CO₂ hydrogenation on Pd/Al₂O₃ catalysts: Kinetics and transient DRIFTS-MS studies. ACS Catal. 5, 6337-6349 (2015).
- C. J. Stalder, S. Chao, D. P. Summers, M. S. Wrighton, Supported palladium catalysts for the reduction of sodium bicarbonate to sodium formate in aqueous solution at room temperature and one atmosphere of hydrogen. J. Am. Chem. Soc. 105, 6318-6320 (1983).
- 67. E. González *et al.*, Hydrogenation of sodium hydrogen carbonate in aqueous phase using metal/ activated carbon catalysts. Appl. Catal. B Environ. 224, 368-375 (2018).
- L. Zhang, M. Zhou, A. Wang, T. Zhang, Selective hydrogenation over supported metal catalysts: From nanoparticles to single atoms. *Chem. Rev.* **120**, 683–733 (2019).
- J. Resasco et al., Enhancing the connection between computation and experiments in electrocatalysis. Natu. Catal. 5, 374-381 (2022).
- M. Peng et al., Fully exposed cluster catalyst (FECC): Toward rich surface sites and full atom utilization efficiency. ACS Cent. Sci. 7, 262-273 (2020).